CONF-800881--2

INTERACTION BETWEEN COMPUTATIONAL MODELLING AND EXPERIMENTS FOR VACUUM CONSUMABLE ARC REMELTING*

MASTER

L.A. Bertram and F.J. Zanner

Sandia National Laboratories
Albuquerque, N.M. 87115

ABSTRACT

A combined computational-experimental modelling effort is currently underway at Sandia National Laboratories to characterize the vacuum consumable arc remelt process. This effort involves the coupling of experimental results with a magnetohydrodynamic flow model which is capable of time accurate solutions of the interdependent fluid flow-solidification process in the ingot. At this time, the modelling and experimental efforts are still in the developmental stage. Therefore, the results presented in this work are intended to provide only a qualitative picture of the Lorentz and buoyancy induced flows.

Models such as this are driven by boundary conditions. Considerable data have been compiled from direct observations of the electrode tip and molten pool surface by means of high speed photography in order to gain an understanding of the processes at the pool surface and the appropriate corresponding boundary conditions. The crucible wall/ molten metal miniscus conditions are less well understood.

Pool volumes are computed at different melting currents and show reasonable agreement with experimentally determined values. Current flow through the ingot is evaluated numerically and the results indicate that a significant portion of the melt current does not reach the interior of the ingot.

* This work supported by U.S. Department of Energy.

DISCLAIMER

I. Introduction. Vacuum consumable arc remelting is a casting process carried out in vacuum with the aim of remelting the consumable electrode in such a way that the new ingot has improved chemical and physical homogeneity. The energy which causes the remelting is supplied by a vacuum arc between the bottom surface of the electrode (cathode) and the ingot top surface/crucible wall (anode); see Fig. 1. Casting rate ("melt rate"), $\dot{m}$, is controlled by varying the melt current, I_m.

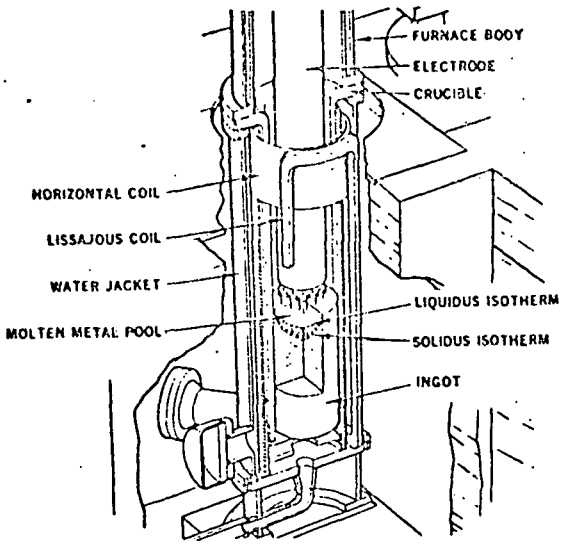

Fig. 1—Vacuum consumable arc remelt furnace cut-away view.

The reason for using this process is to increase the homogeneity of the resulting ingot. However, its application is limited by the onset of significant macrosegregation in segregation sensitive alloy systems. Since increasing the ingot diameter will increase the propensity for macrosegregation, segregation sensitive alloys are limited to small ingot diameters. This limitation is believed to be caused by adverse fluid flow and solute transport within the melt pool and the ajacent interdendritic region. The goal of the research program described below is to understand how melt parameters such as I_m relate to fluid flow, solute transport, and the resulting ingot homogeneity.

The U-6w/oNb alloy used in this research was chosen because of the following properties:

(i) intense macrosegregation is observed in small diameter ingots (0.208m).

(ii) Niobium is completely soluble in both liquid and solid uranium near the solidification temperature range.

(iii) Niobium diffusion in solid uranium is low.

In particular, the macrosegregation observed in U-6w/oNb VAR ingots can be broken down into three types. First, and most conspicuously, (Fig. 2), bands of varying concentration can be seen. Second, the composition of the alloy can vary with distance from the axis (Fig. 3). Finally, the ends of the ingot may have different solute contents than the interior, which was formed under quasi-steady solidification conditions.

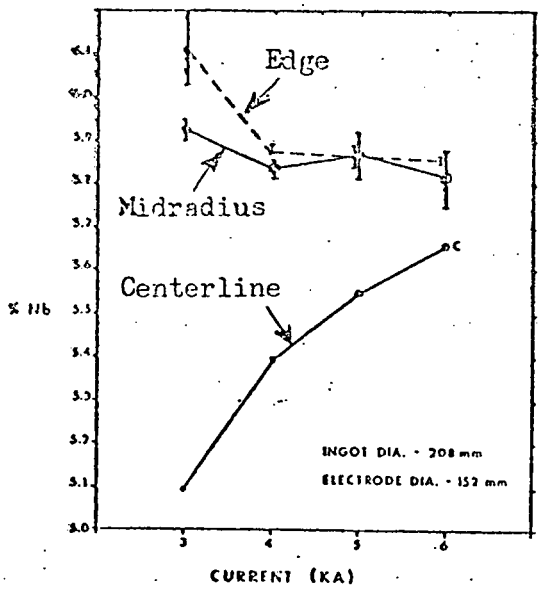

Fig. 3. Centerline to edge macrosegregation in the ingot of Fig. 2, as a function of melt current.

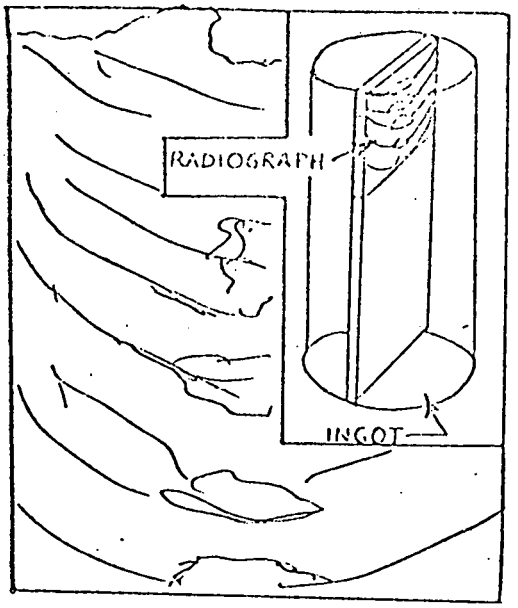

Fig. 2. Positive radiograph of 7&1 cm-dia (0.254m) ingot. No content varies from w/o inside bars to w/o between bars.

4/5 8.5

The actual development of macrosegregation clearly must be a consequence of the conditions on the moving solid-liquid interface in the ingot. As shown by Flemings, Mehrabian, and others [1,2,3] over the past several years, a quantitative connection can be made between the flow and the thermal environment in the interdendritic spaces of the "mushy zone". However, this theory requires that these conditions be determined with great precision and detail in order that predictions of macrosegregation become possible. It is this requirement of great detail and the accompanying wish to maximize reliability and relevance of conclusions which have motivated the combined numerical (detailed) and experimental (reliable, realistic) analysis of VAR.

At this time, the modeling and experimental efforts are still in the developmental stage, so the results presented here are intended to provide only a qualitative picture of the Lorentz and buoyancy induced flows in the region ahead of the dendrites and in the part of the mushy zone where they are very coarse (volume fraction solid $g_s \lesssim 0.5$).

Basically, the Sandia VAR research program is driven by the data obtained from an instrumented 10-in (0.254m), highly coaxial (axisymmetric) furnace. The instrumentation is briefly described in Section II, followed in Section III by the formulation of a magnetohydrodynamic flow model. The model

is capable of time-accurate simulations of the coupled convection-solidification processes in the ingot. Section IV describes experiments from which "first-generation" boundary conditions are constructed and presents the resulting boundary conditions. Finally, in Section V a parameter study using the model produces predicted pool volumes as a function of melting current and measured melt rate. These calculated volumes are compared to experimentally determined values in order to infer the fraction of current passing through the melt pool.

II. Experimental facilities. The basic measurements made on the furnace when it operates in a normal production mode (as depicted in Fig. 1) consist of melt current I_m, voltage across the bus bars V_m, furnace pressure p_m, and furnace gas composition. Melt current is measured with a shunt in series with the negative bus bar and simultaneously by a Hall-effect transducer; both I_m and V_m are recorded at a 5kHz resolution on magnetic tape and are subsequently analyzed on a minicomputer. Furnace gas composition is obtained from a mass spectrometer which obtains its samples through a differentially pumped quartz tube with a 0.015-in (0.00038m) orifice placed approximately 3 in (0.076m) above the finished ingot's top surface in the annulus between the electrode and crucible.

For obtaining heat transfer data, the water jacket water flow is monitored using an orifice plate flowmeter. Thermocouples placed at the inflow and outflow ports of the jacket provide data on temperature rise of the cooling water, and thus, on the global heat removal rate through the crucible. In addition, thermocouples can be placed in various positions on the outside of the copper crucible wall without affecting the melting process. These yield details on the distribution of the crucible-cooling water heat transfer.

While all the above-described measurements are conveniently made during production melting conditions, none allows direct observation or measurement of the active zone of the VAR furnace; namely, the interelectrode gap in which the arc operates and across which metal must be transferred from the electrode to the melt pool atop the ingot. To obtain such data, experimental melting is performed in a modified arrangement of the standard furnace (Fig.4). The modification consists of inserting an additional section of vacuum chamber, with independent cooling, sight ports, and instrument ports, between the crucible flange and the furnace body; inside the crucible itself a moveable stool ("retractable hearth") is mounted on a hydraulically-driven screw mechanism which can withdraw it at the rate new ingot forms. This retractable hearth

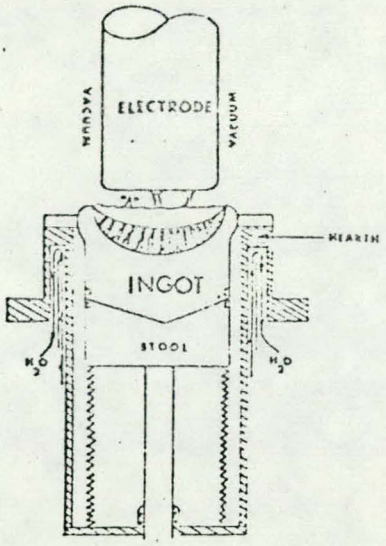

(a)
Figure 1. Retractable Hearth Schematic

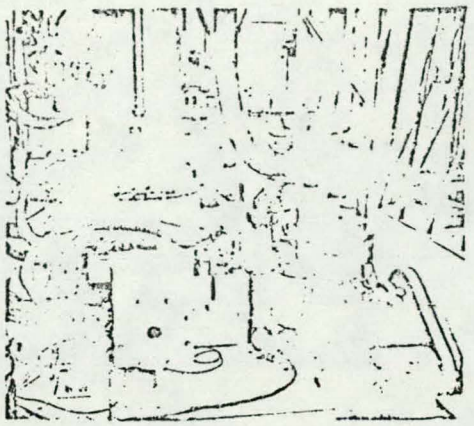

(b)
Figure 2. Melting Chamber and Observation Port

Fig. 4. The Sandia retractable hearth apparatus.

arrangement allows long-term observation of the interelectrode gap since electrode feed and ingot withdrawl can be matched so that the gap remains in the field of view. The sight ports of the chamber are arranged for both direct viewing across the gap, and for oblique viewing of a large fraction of the pool surface (the electrode blocks a full view of the surface). Both high-speed color movies (~10,000 frames/sec) and color still photographs have been made in this way.

Besides these measurements made at Sandia National Laboratories, an important additional source of data has been the Union Carbide Nuclear Divisions's Y-12 plant. This support consisted of melting an 8-in (0.208m) uranium-6w/o niobium ingot, sectioning the resulting material, and doing radiography on the sections (Fig. 2 is a positive taken from these radiographs). For the reasons noted in the Introduction, the U-Nb system is ideal for segregation studies, so the majority of the analysis done to date has involved this ingot.

For the radiographic information to be reduced to quantitative data, it is necessary to combine specimen thickness information, calibration of the photographic emulsions (provided by step wedges of pure U and of U-6w/oNb which were radiographed along with the specimens), and the raw radiographs to calculate pointwise densities. This is currently being done by computer based image processing techniques. More detailed descriptions of experimental apparatus and technique is found in the references[4,5,6].

Fortuitously, the strong banding of this alloy provides an additional datum; namely, if it is true that the bands are created during the latter stages of solidification, then they serve as reliable markers of the outline of the melt pool at the time of their formation. To be precise, what the bands represent is contours of some fraction solid (not, of course, $g_s = 1$, the solidus). In this report, "measured pool volume" will refer to the volume enclosed by the solid of revolution generated by a band and the plane through the intersections of the band with the edge of the ingot.

III. Mathematical model. In order that the numerical model have as simple a form as possible while retaining the relevant physics for the determination of the macroscopic heat and fluid transfer, the following forms of the governing equations are applied:

$$\frac{\partial \zeta}{\partial t} + \frac{\partial(u\zeta)}{\partial x} + \frac{\partial(v\zeta)}{\partial r} = Pr\left[\frac{\partial^2(\nu\zeta)}{\partial x^2} + \frac{\partial}{\partial r}\left(\frac{\partial(r\nu\zeta)}{r\partial r}\right) + S \right] + Pr^2 Gr \frac{\partial \theta}{\partial r} - \frac{1}{A_o^2}\frac{\partial B^2}{r\partial x} \quad (1)$$

with $S = 2\left(\frac{\partial v}{\partial r} - \frac{\partial u}{\partial x}\right)\frac{\partial^2 \nu}{\partial x \partial r} + 2\left(\frac{\partial u}{\partial r}\frac{\partial^2 \nu}{\partial x^2} - \frac{\partial v}{\partial x}\frac{\partial^2 \nu}{\partial r^2}\right)$;

$$\frac{\partial h}{\partial t} + \frac{\partial(uh)}{\partial x} + \frac{\partial(rvh)}{r\partial r} = \frac{\partial}{\partial x}\left(\kappa \frac{\partial h}{\partial x}\right) + \frac{\partial}{r\partial r}\left(r\kappa \frac{\partial h}{\partial r}\right) + \frac{j^2}{\Sigma} \quad (2)$$

$$\frac{\partial^2 \psi}{\partial x^2} + r\frac{\partial}{\partial r}\left(\frac{\partial \psi}{r\partial r}\right) = -r\zeta \quad (3)$$

$$u = \frac{\partial \psi}{r\partial r} \qquad v = -\frac{\partial \psi}{r\partial x} \quad (4)$$

where (x,r) are the axial and radial cylindrical coordinates (scaled) by ingot radius R having origin on the melt pool axis at the surface; t is time, scaled by R^2/κ_o, κ_o being the reference value of the thermal diffusivity; ζ is vorticity, $= \partial v/\partial x - \partial u/\partial r$ in terms of the velocity components (u,v); A_o^2 is the square of an Alfvén number based on thermal diffusion speed, $A_o^2 = (\kappa_o/R)^2/(B_o^2/\mu\rho_m)$; B is the magnetic induction azimuthal component scaled by $B_o = \mu I_m/2\pi R$; θ is temperature difference from the mid-mushy zone temperature $T_o = \frac{1}{2}(T_L + T_s)$, scaled by $\Delta T_o = \frac{1}{2}(T_L - T_s)$ with $T_{L,s}$ being respectively liquidus and nonequilibrium solidus temperatures; Pr is Prandtl number, ν_o/κ_o with ν_o being a reference

kinematic viscosity of the liquid metal; Gr is Grashof number = $g\alpha\Delta T_o R^3/\nu_o^2$ with g being acceleration due to gravity and α being the volumetric coefficient of thermal expansion of the liquid; h is the enthalpy, scaled by $\frac{1}{2}L$ with L being the latent heat of fusion; j is current density, scaled by $I_m/\pi R^2$; and Σ is a Joule heating parameter, $\Sigma = \rho_m L\sigma\kappa_o R^2/2I_m^2$ with ρ_m being mass density and σ the electrical conductivity of the liquid. The function $\psi(x,r,t)$ is the streamfunction, introduced to obtain exact conservation of volume. When the flow is steady, contours of constant ψ ("streamlines") are also particle paths. The only variation in mass density considered is contained in the term of (1) multiplied by Gr, which assumes that $\hat{\rho}_m = \rho_m(1-\alpha[T-T_r])$, T_r being some reference temperature in the liquid ("Boussinesq approximation").

The essential physics of the problem can be seen in equation (1), where the rightmost pair of terms represent the sources of vorticity due to radial temperature gradient $\partial\theta/\partial r$ and axial magnetic pressure gradient $\partial B^2/\partial x$, respectively. The two terms are of opposite sign, and are of almost exactly the same magnitude for the ingot sizes considered here. Thus the net motion is determined as the result of near-total cancellation of these two opposing driving forces (buoyancy and Lorentz forces).

Accompanying equations (1)-(4) are the following equations of state.

$$\kappa(\theta) = c_L k(\theta)/|\nabla h|/|\nabla T| \qquad (5)$$

with the $|\nabla h| / |\nabla T|$ value being calculated from the points in the neighborhood rather than specified as a function of θ, and with k being the dimensionless thermal conductivity, with $c_L = 2C_{po}\Delta T_o/L$, and C_{po} being a reference specific heat (the same value used in defining κ_o);

$$\nu = \nu(\theta) \qquad (6)$$

being given as a closed-form function (curve fit); and finally,

$$h = h(\theta) \qquad (7)$$

is specified as an "average" nonequilibrium cooling history by assigning the regular-mixture enthalpy of the components (liquid and solid) which would be present according to the Scheil microsegregation equation[7]. Rather than calculating the Scheil prediction of fraction liquid and the solid composition every time an enthalpy value is desired, the curve $h(\theta)$ is computed once and a piecewise linear curve fit is made to it. This linear function is then used to assign $h(\theta)$[6].

Equations (1)-(7) are solved numerically in a rectangular region representing a cross section of the ingot top (Fig. 5). The actual numerical operations consist of solving the two parabolic equations (1),(2) by an explicit, conservative, upwind-differenced scheme, and then performing a symmetric successive over-relaxation on the elliptic equation (3); for efficiency, these steps are carried out in analytically strained cylindrical coordinates[6].

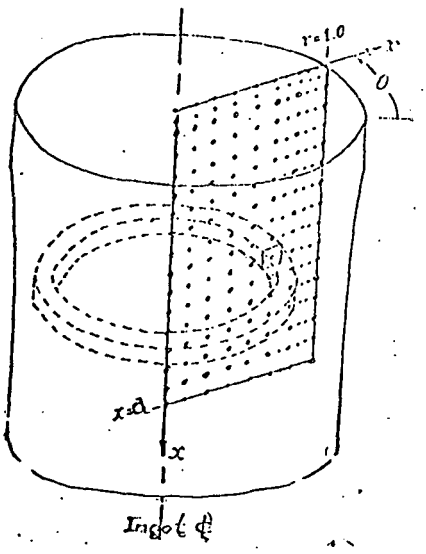

Fig. 5. Coordinates and finite difference grid for numerical solutions.

Explicit field equations for the electromagnetic variables B and j are not included because these have been treated by a fully decoupled magnetostatic approximation. This is possible because of the small size of the ingots and the low fluid velocities which together imply small magnetic Reynolds number $Rm = U_o R \mu \sigma$; and thus, small induced fields.[9] In particular, the dimensionless azimuthal magnetic induction vector component is taken to be:

$$B(x,r) = \frac{J_1(\beta_o r)\cosh\beta_o(a - x)}{J_1(\beta_o)\cosh\beta_o a} C_B \qquad (8)$$

where a is the aspect ratio of the computational zone (Fig. 5), $J_1(\cdot)$ is the Bessel function of order one, and β_o is the first zero of the zero-order Bessel function. Once B(x,r) is given, Ampere's equation determines j(x,r). Note that a parameter $0 \leq C_B \leq 1$, the fraction of melt current passing through the pool, has been inserted because the detailed current budget in a VAR furnace has not been measured to the authors' knowledge.

IV. Boundary conditions. (a) Initial experiments. The facilities described in Section II have yielded a mixture of qualitative and quantitative information concerning the VAR process. From the retractable hearth experiments[5,8], which were all done with stainless steel or superalloy ingots, direct observation has determined that the mode of metal transfer is chiefly bulk liquid transport; that individual vacuum arcs behave as they do in vacuum switches, etc. (i.e.,

individual cathode spots are created near the centerline of the electrode face, do a high-speed random walk with a mean radial speed of about 10^2 m/s, and are extinguished at the edge of the electrode, or, in some cases, on the lateral surface of the electrode); that the bridging of the electrode gap by a liquid droplet causes immediate (on time scales shorter than 10^{-4}s) extinguishing of all cathode spots, so that all melt current must pass through the resulting "molten wire" between the electrodes; and that both pool surface and electrode surface are at low uniform superheats, probably $< 200K$[6]. An immediate consequence of these observations is a strategy for controlling electrode gap based on analysis of the electrical waveforms $V_m(t)$[8].

Along with these observations, crucible and water jacket thermocouple measurements have been made during melts of stainless steel (See Fig. 6). This quantitative data indicates that the significant heat removal from the ingot

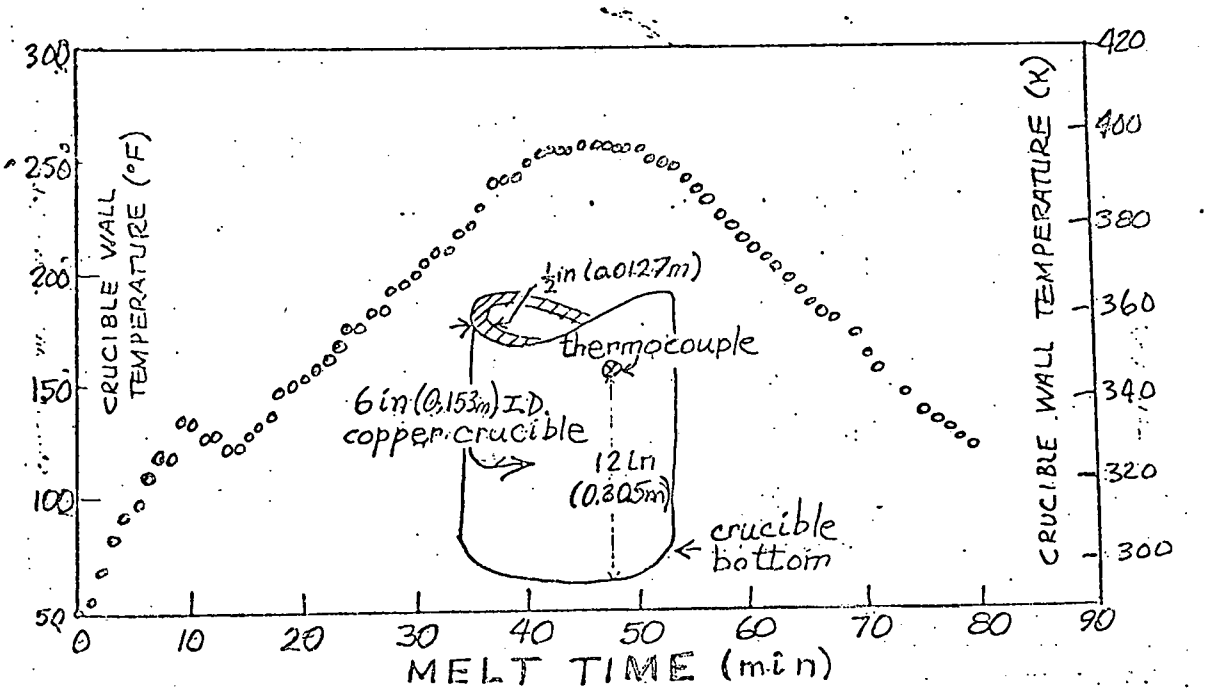

Fig. 6. Measured temperatures on crucible wall during 304L stainless steel melting. Ingot growth rate 0.22 in/min (9.3×10^{-5} m/s).

occurs in a very narrow band of contact on the crucible wall and that the electrical energy input rate is nearly matched by the rate of thermal energy removal by the cooling water (after the startup transient, under constant current I_m melt conditions).

(b) Initial numerical boundary conditions. Taken together, these observations and measurements suggest the following boundary conditions. First, the low

observed superheats suggest

$$T^*(x=0,r,t) = T_L + \Delta T_S^* H(R_e - r) \tag{9}$$

where $H(R_e - r) = \begin{cases} 1 & r \leq R_e \\ 0 & r > R_e \end{cases}$ is the Heaviside unit step function

and ΔT_S^* is the superheat of the pool surface directly under the electrode (the value used in the calculations given below was $\Delta T_S^* = 122K$). The surface also requires a streamfunction boundary condition (uniform inflow was used since pool velocities so greatly exceed inflow velocity) and a vorticity boundary condition (which was taken to be zero vorticity assuming that no net shear stress is applied to the pool surface). These conditions are

$$\psi(x=0,r,t) = \psi_1 r^2 \tag{10}$$

and

$$\zeta(x=0,r,t) = 0 \tag{11}$$

where $\psi_1 = u_o^*/(2\kappa_o/R)$ is a Peclet number based on average inflow speed $u_o^* = \dot{m}/\rho_m \pi R^2$.

On the lateral surface of the ingot (crucible wall), the flow conditions are the usual:

$$\psi(x,r=1,t) = \psi_1 \tag{12}$$

ζ is derived from $\partial u/\partial r)_{r=1}$ unless solidification has occurred at $r < 1$. (13)

The thermal boundary conditions at the wall are not so easily determined. The data measured on the outside of the crucible has a good deal of the detail smeared out by diffusion, and this detail cannot be restored by analytical means since this restoration would be a classical ill-posed boundary value problem. The situation is further complicated by the fact that the crucible wall temperatures indicate that heat transfer is probably a combination of film cooling and nucleate boiling. Thus, exterior crucible wall data alone are not sufficient to provide a reliable accurate boundary condition. Furthermore, the detailed analysis discussed by Wray earlier in this meeting [10] indicates that the behavior of the ingot-crucible contact is at least as complicated as the crucible-cooling water contact. A crude parameterization of the expected temperature dependent ability of the ingot to reject heat to the cooling water has been used, with parameter values estimated rather than measured. Specifically, the contact zone

is assumed to have a thermal resistance which varies with local temperature (see Fig. 7):

$$-k^* \frac{\partial T^*}{\partial r^*} = \varepsilon \sigma^* T_w^{*4} + \frac{T_w^* - T_{H_2O}^*}{R_T} \tag{14}$$

where the "w" subscript denotes "wall" values, and H_2O refers to the cooling water. The thermal resistance is defined in Fig.7; this form of R_T is chosen so that the minimum resistance R_o operates when temperature is above T_{RO}; weakening contact stress causes increasing R_T for intermediate temperatures; and, finally, conduction ceases below T_R when thermal contraction has caused the ingot to shrink out of contact with the wall entirely. Parameter values assigned have been: $R_o = 1.0 W/cm^2\text{-}K$ (about four times the thermal resistance of the copper crucible alone); $T_{RO} = T_s$, the nonequilibrium solidus temperature; $T_R = T_s - 10^{-3}/\alpha_s$ where α_s is the volumetric coefficient of thermal expansion of the solid. This T_R means that the solid has undergone a 0.1% volumetric contraction at the break of wall contact; for U-6w/oNb alloy T_R was 200K below T_s.

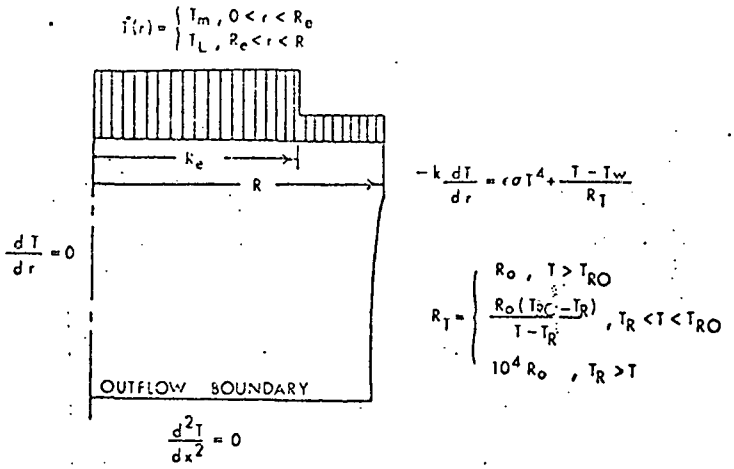

Fig. 7. Thermal Boundary Condition Summary (See text for notation).

On the axis of the ingot, symmetry provides boundary conditions unambiguously:

$$\psi(x, r=0, t) = 0 \tag{14}$$

$$\zeta(x, r=0, t) = 0 \tag{15}$$

$$\frac{\partial Q}{\partial r}(x, r=0, t) = 0. \tag{16}$$

At the bottom of the computational mesh, typical "outflow" boundary conditions are given on streamfunction and enthalpy:[11]

$$\frac{\partial^2 h}{\partial x^2}(x=a, r, t) = 0 \tag{17}$$

$$\frac{\partial^2 \psi}{\partial x^2}(x=a, r, t) = 0 \tag{18}$$

and vorticity is zero because the code forbids melting on the outlflow boundary.

At interior solid surfaces (taken here to be points for which θ first drops below 0.333; i.e., where the Scheil equation first indicates that fraction solid exceeds 0.55), the streamfunction is specified to be rigid body motion

$$\psi = \psi_1 r^2 \tag{19}$$

and vorticity is computed from[11]

$$\zeta = \frac{\partial v_t}{\partial n} \tag{20}$$

where n is the normal to the solid surface (immobilization isotherm) pointing into the melt, and v_t is the velocity tangential to the surface at the ajacent liquid mesh point.

V. Limited experimental and computational results. To briefly recapitulate the above, then, direct observation of the electrode gap region has produced several qualitatiive and quantitative improvements in the understanding of the VAR process. The most important of these have perhaps been the observations of the transfer of metal from the consumable electrode to the pool by the bridging of the gap with liquid metal droplets, and the synchronization of these events with the characteristic millisecond lifetime waveforms of the furnace electrical signal[4,5,8]. These observations have clearly established that the bulk of metal transfer is by liquid flow, and that, when a droplet shorts across the gap, all arcs are extinguished.

These observations have also suggested the boundary conditions detailed above in equations (9)-(20) for the ingot top. With these conditions as input, along with the melting rates $\dot{m}$ obtained simply by dividing the total ingot weight by melt time, it is possible to produce numerical models corresponding to the experimental melts. The utility of these models consists mainly in providing a base for a parameter sensitivity study as well as some qualitative insight into the phenomena which may occur in the system when it is driven by realistic inputs. Quantitatively, the only meaningful comparison which can now be made with the observations is computed vs. measured pool volumes (see Fig. 8). The computed volume is that enclosed by the immobilization isotherm, and thus represents a lower bound on the volume which is enclosed by a band formed at a temperature between immobilization ($\theta_I = 0.333$) and nonequilibrium solidus ($\theta_s = -1.0$).

While the numerical model produces reasonable volumes at each current level of the experiment for $I_m \leq 5$kA, it cannot produce a bounded pool volume at $I_m = 6$kA because the Lorentz force is so dominant that heat transfer to the crucible by convection is greatly enough impeded that the melt pool depth exceeds the length of the computational mesh (about 1.33 radii). Clearly, either $C_B \neq 1.0$, or the current path through the ingot is not accurately given by eq.(8). Present evidence indicates that both assumptions need to be examined carefully.

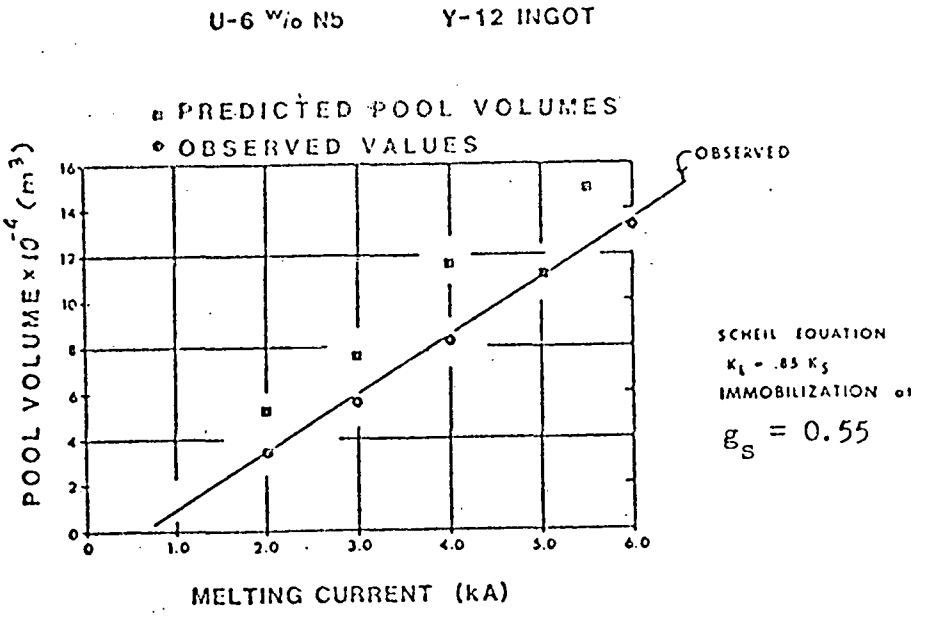

Fig. 8. Computed vs. measured pool volumes as functions of melt current. All current passing through pool ($C_B = 1.0$ in eq.(8)).

A simple numerical experiment can serve to obtain an estimate of C_B which would be appropriate to the current model in (8). Suppose first that a continuous caster is to be run at the same rate as the VAR ingot at 6kA (205g/s; 3.25×10^{-4} m/s); there would be no Lorentz force in the absence of current passing through the pool. The resulting motion in the melt pool would, of course, be upward along the axis and downward along the cold outer edge of the pool. This is the usual thermal convection circulation due to buoyancy forces acting along (see Fig. 9).

Next, consider the case in which a small current, say 1kA, is passed through the pool. In this case the Lorentz force, though weak, opposes the buoyancy force and slows the convective motion. However, despite the slight drop in maximum velocity, convection still totally dominates the heat transfer and pool shape (isotherm shape in general) is not affected. In fact, it requires a current strong enough to essentially cancel the buoyancy force before a noticeable change is produced in the isotherms.

This threshold is crossed at $I_m \simeq 1.75$ kA; until about 3.25 kA, the buoyancy and Lorentz forces virtually cancel one another, and the net

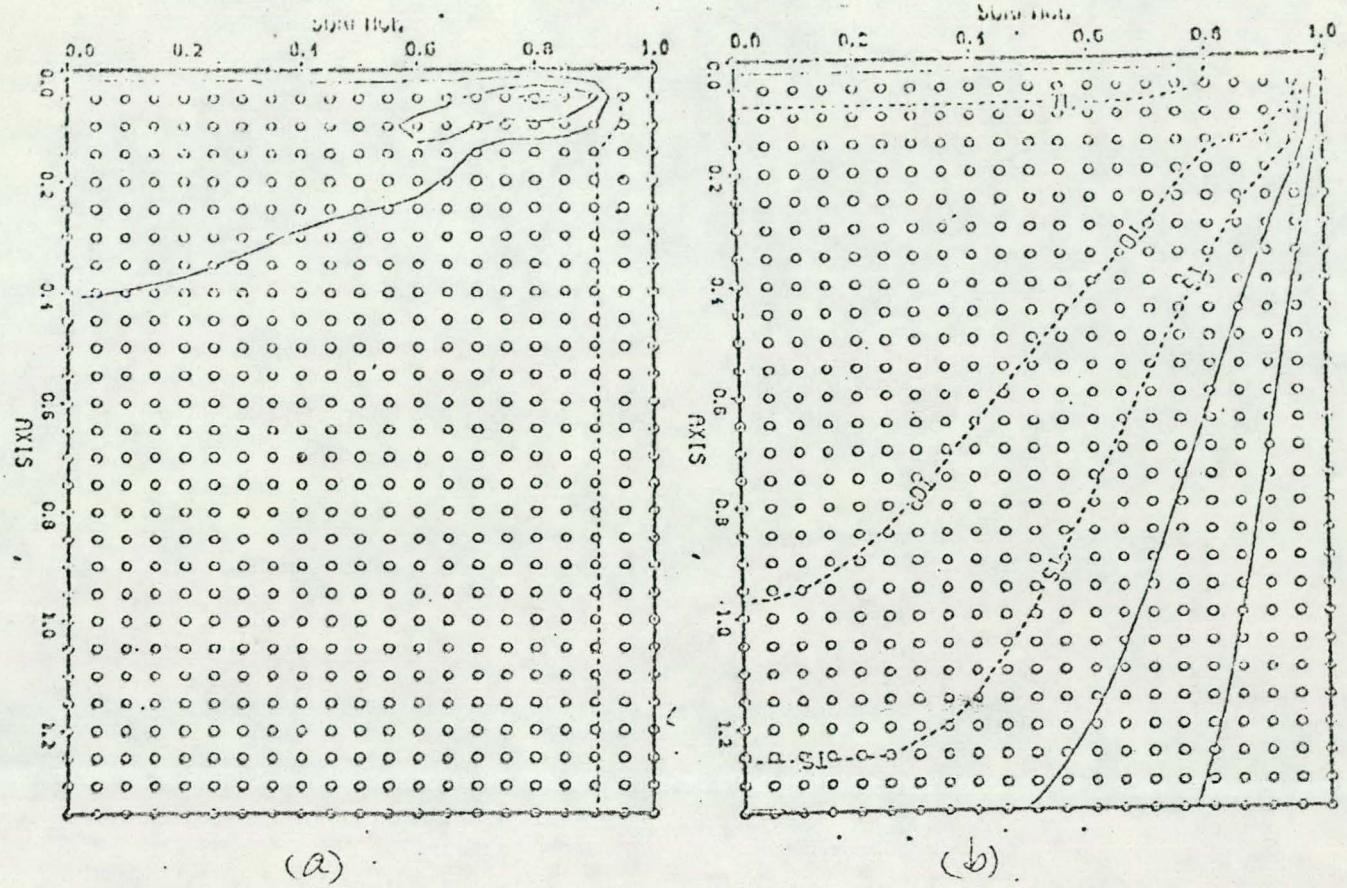

Fig. 9. Calculations for U-6w/oNb alloy, 205g/s melt rate, 6-in (0.156m) electrode, 8-in (0.208m) ingot. Zero pool current case.
(a) Streamlines with $\Delta\psi = 2.0$ (b) Isotherms with $\Delta T = 80K$.

motion is weaker by nearly an order of magnitude than the motion in the unopposed thermal convection case.(note that the spacing of streamfunction contours, which is a rough measure of velocity magnitude according to eq.(4), has dropped from 2.0 in Fig. 9 to 0.4 in Fig. 10). Throughout this current range, the weaker flows result in deeper pools. At 2.5 kA pool current, the motions consist of separate zones of magnetic and thermal circulations (Fig. 10); furthermore, there is evidence of long transient times for disturbances to these flows, so their stability appears to be just about marginal.

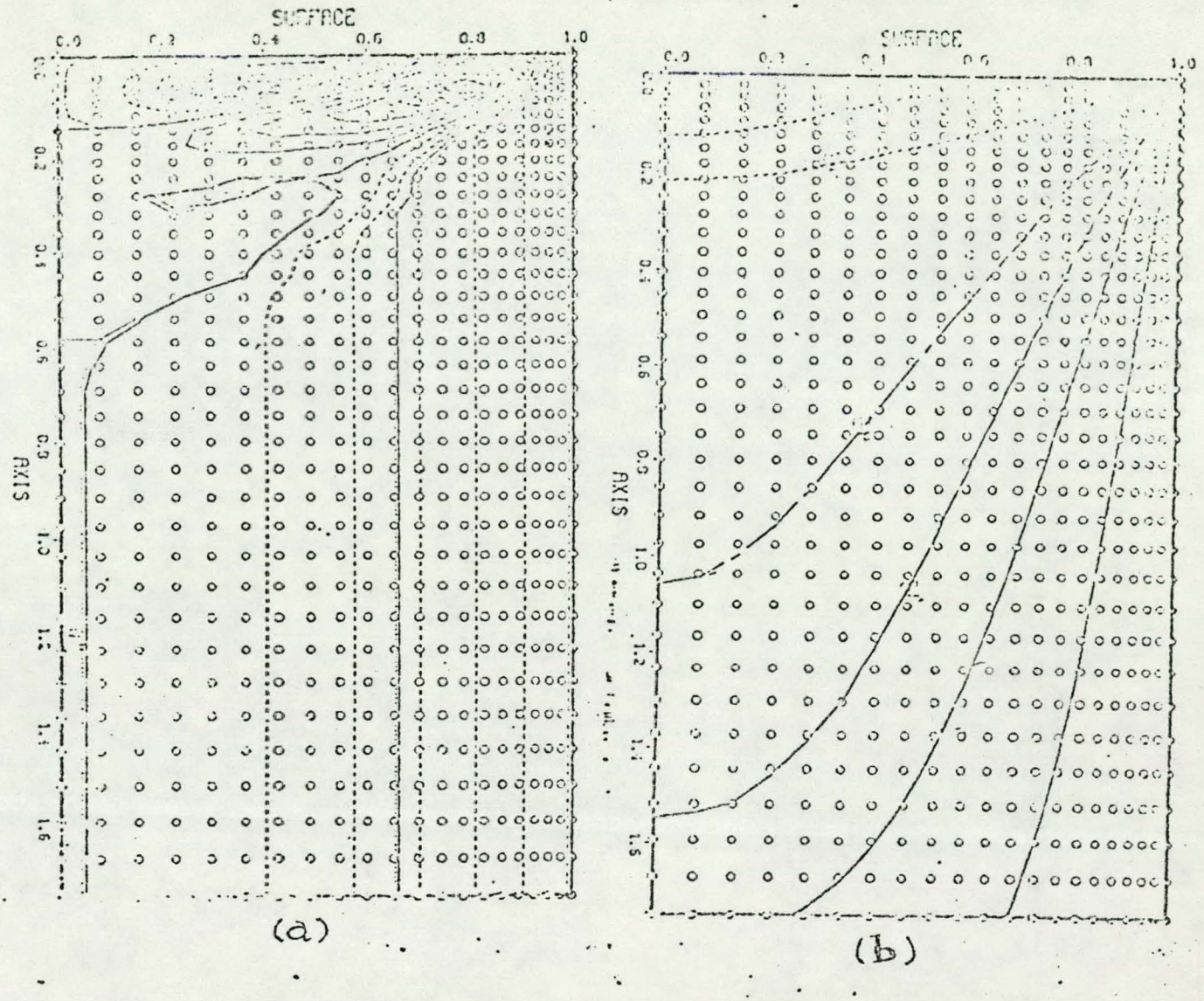

Fig.10. Calculated flow under same conditions as Fig. 9, except that pool current is 2.5 kA. (a) Streamlines with $\Delta\psi = 0.4$ (b) Isotherms with $\Delta T = 80K$.

When the current level becomes high enough, the Lorentz forces will dominate the pool dynamics, and circulations will be mainly counter to the thermal convection circulation direction. This must result in enhanced gradients of temperature at the edge of the dominant cell, so that a thermal cell will always appear at the pool edge. Maximum velocities must again increase, but with a reverse sense from the buoyancy-dominated case. This has the effect of reducing convective heat transfer, and thus increases the depth of the pool dramatically. In fact, 3.5 kA is sufficiently high current to cause even an extended (1.75 radii) computational zone to become mushy to its bottom (Fig. 11).

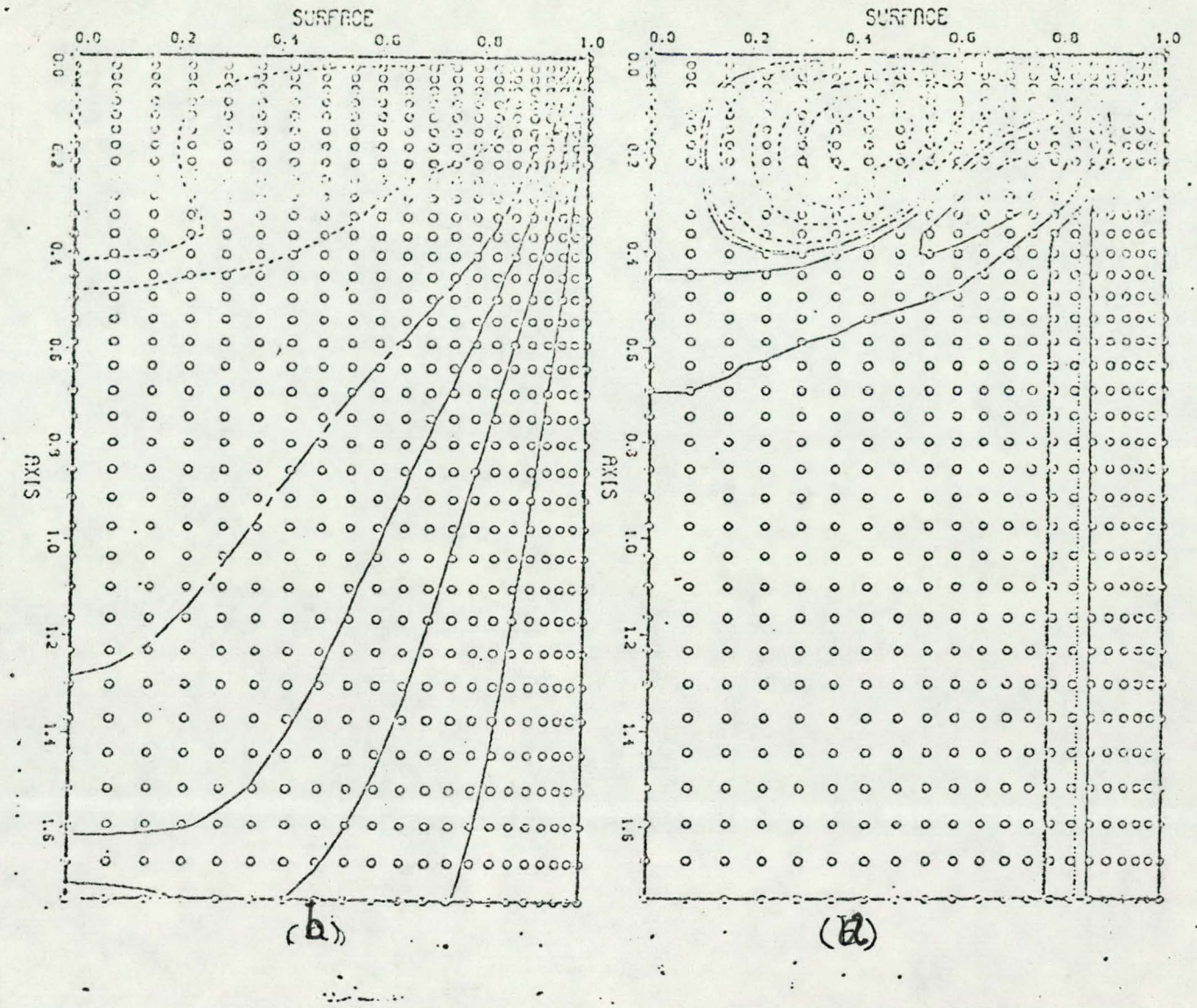

Fig. 11. Calculated flow under same conditions as Fig. 9, except that pool current is 3.5 kA. (a) Streamfunction with $\Delta\psi = 3.0$ (b) Isotherms with $\Delta T = 80K$.

Now, these calculations each give a pool volume prediction which may be plotted vs. pool current (Fig. 12). The curve appears to be monotonically increasing in pool current, as one would expect since increased current means increasingly strong inhibition of heat transfer from the pool. The observed pool volume at 6 kA cuts this curve at the right hand end, indicating that a current of $I_p = 3.3$ kA would reproduce the observed volume. Thus, for current distribution given by equation (8), $C_B = 0.55$ would seem to be appropriate at the $I_m = 6$ kA melt current level.

From this and similar parameter studies using the mathematical model, those parameters which significantly affect the behavior of the ingot

can be isolated much more economically than by experimentation. The above example indicates the need for accurate inputsffor the boundary conditions at the ingot meniscus-crucible wall contact, for accurate determination of current paths, and for accurate determination of the thermal loading of the pool surface by plasma and radiation as well as by the conventional liquid transfer. At the same time, any changes made in estimated values of the parameters must be consistent with the observations already made and with such global constraints as overall energy budget balance.

Specific experiments suggested by this first-generation model consist of:

(i) Measurement of surface temperatures in the retractable hearth.

(ii) Measurements of surface velocities in the retractable hearth.

(iii) Measurements of crucible wall heat fluxes in the production configuration.

(iv) Measurements of anode current partitions between crucible wall and pool surface, to improve eq. (8) and to fix C_B.

This experimentation must be accompanied by the corresponding arc physics analysis, fluid dynamics analysis, electromagnetic analysis, etc., to assure consistency; see Fig. 13.

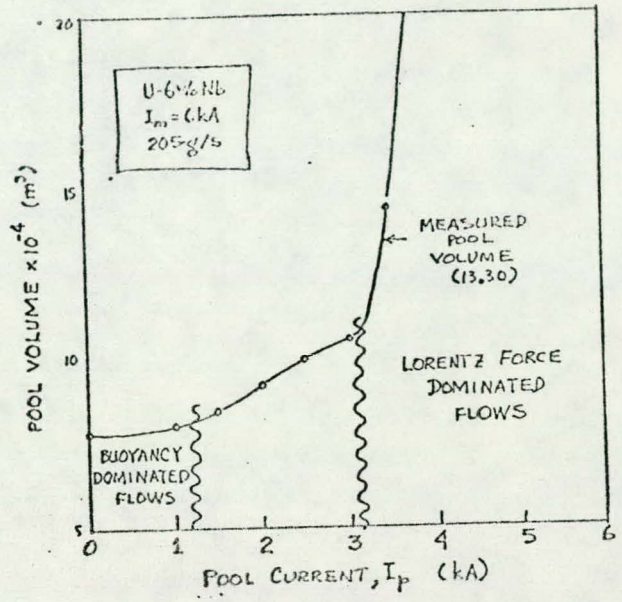

Fig. 12. Pool volume as a function of pool current at fixed melt rate as a means of estimating the fraction of current passing through melt pool.

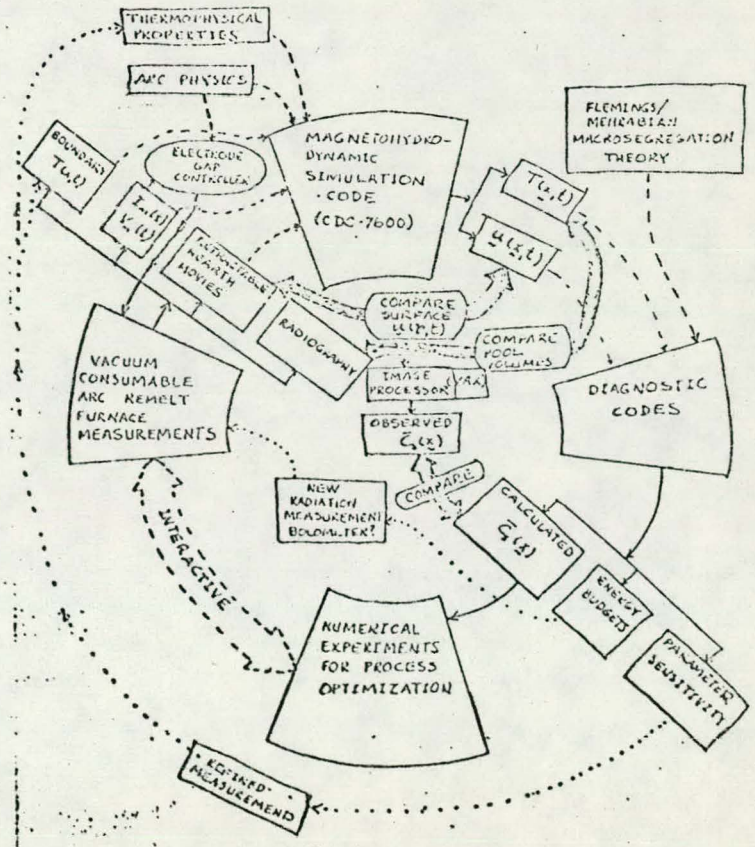

Fig. 13. SANDIA VAR PROGRAM

V. Summary. At the outset, the goal of this program was stated to be application of the Flemings-Mehrabian macrosegregation theory to the modelling of macrosegregation in VAR ingots. Because the interaction between the experiments and the model has not yet yielded a well-focussed picture of the motions in the ingot or of the boundary conditions which produce them, the attempt has not yet been made to incorporate the equations of the macrosegregation theory into the model. When that step can be carried out with some confidence, process optimization can be undertaken (Fig. 13). At present, it is clear that the immense complexity of the physics of the process requires continuation of the intimate step-by-step interdependence of the modelling and experimental results to keep the former realistic and the latter comprehensible.

ACKNOWLEDGEMENT

The authors are indebted to Drs. R.Mehrabian (National Bureau of Standards), G.W.McClure and B.Marder (both of Sandia National Laboratories) for helpful discussions involving macrosegregation and arc physics as related to the vacuum consumable arc remelt process.

Dave Beck at Union Carbide's Y-12 facility provided valuable experimental support, as did Robert Fisher, Alan Netz, and James Maroone at Sandia National Laboratories.

REFERENCES

(1) Flemings, M.C. and Nereo, G.C.: Trans.TMS-AIME, 1967,212,1449.

(2) Mehrabian,R.,Keane,M., and Flemings,M.C.:Met.Trans. 1970,1,3238.

(3) Fujii,T.,Poirier,D.,and Flemings,M.C.:Met.Trans. 1979,10B,331.

(4) Zanner, F.J.: Met.Trans. 1979,10B, 133.

(5) Zanner,F.J.: Proc. 6th Internat. Vac. Met.JConf. 1979,417.

(6) Zanner, F.J.,and Bertram L.A.:SAND80-1156 "Computational and Experimental Analysis of a U-6w/oNb Vacuum Consumable Arc Remelt Ingot", Sandia National Laboratories, 1980.

(7) Scheil,E.:Z.Metallk. 1942, 34, 70.

(8) Zanner, F.J.:"The Influence of Electrode Gap on Drop Short Properties During Vacuum Consumable Arc Remelting", submitted to Met.Trans.B.

(9) Bertram, L.A.:Proc. 1st Internat.Conf.Math.Model. 1977,Vol.III,1173.

(10)Richmond,O.and Wray,P.: at Engineering Foundation Conference on Modelling of Casting and Welding Processes, . Rindge, N.H. 1980.

(11) Roache,P.J.:Computational Fluid Dynamics, Hermosa Press, Albuquerque N.M. 1976.